International Journal of Heat and Mass Transfer 173 (2021) 121235

Contents lists available at ScienceDirect

International Journal of Heat and Mass Transfer

journal homepage: www.elsevier.com/locate/hmt

Thermal transport in pristine and defective two-dimensional polyaniline (C_3N)

Xin Wu [a], Qiang Han [a,*]

Department of Engineering Mechanics, School of Civil Engineering and Transportation, South China University of Technology, Guangzhou, Guangdong Province 510640, People's Republic of China

ARTICLE INFO

Article history:
Received 18 January 2021
Revised 2 March 2021
Accepted 16 March 2021

Keywords:
Two-dimensional polyaniline
Thermal transport
Structural defects
Molecular dynamics
Graphics processing units

ABSTRACT

Two-dimensional polyaniline (2D-PANI) with semiconductor properties, a single crystalline carbon nitride with a stoichiometry of C_3N, has attracted a lot of interest after its successful synthesis. In this study, the thermal transport properties in pristine and defective 2D-PANI were explored by extensive molecular dynamics (MD) simulations. Results based on three different versions of the MD method consistently showed that the lattice thermal conductivity of the pristine 2D-PANI is up to around $2000 Wm^{-1}K^{-1}$. It decreases significantly after the introduction of structural defects and is essentially in a low-power law with the defects concentration. In addition, the difference in the weakening of thermal conductivity between vacancy and topological defects stems mainly from their respective differential effects on the low-frequency out-of-plane phonons. Remarkably, it also reveals the potential mutual constraints between anharmonic phonon-phonon scattering and phonon-defect scattering. These findings provide guidance for the thermal management of 2D-PANI-based electronic devices and are also expected to advance their application in the field of thermal design of nanomaterials.

1. Introduction

At a stage in history when science and technology are advancing at a rapid pace, mankind is leading and witnessing the constant transformation and development of various emerging technologies. Easily overlooked but pivotal, the materials industry, behind the booming tide of technology in all fields, provides an ideal platform and strong support for the development of technology. Two-dimensional (2D) materials stand out among the many new materials with their mere mono-atomic thickness. With graphene [1] as a precursor, one can list hexagonal boron nitride [2], boronene [3], and a family of transition metal dichalcogenides (TMDs) represented by MoS_2 [4]. Over the years, it is undeniable that carbon-based materials in various fields have remained leaders in advanced materials, and therefore 2D carbon nitrides, as a class of their derivatives, have gained a lot of popularity. Graphitic carbon nitride nanofilms with semiconductor electronic properties ($g-C_3N_4$) [5], 2D structures with ordered distribution of holes and nitrogen atoms (C_2N) [6], and graphene-like 2D polyaniline (2D-PANI) semiconductor structures with a stoichiometry of C_3N [7] have all been experimentally synthesized in recent years and have been proven that they have great potential in energy storage, catalysis, and new electronic devices.

Among the above-mentioned graphene-based 2D carbon nitrides, 2D-PANI has the optimal energy stability due to its pristine structure without cavities [8]. Furthermore, from the perspective of atomic modification, 2D-PANI can be seen as the product of selective substitution of carbon atoms in the graphene by nitrogen atoms, which is widely considered to be an effective way to improve the electronic and optoelectronic properties of graphene. The nitrogen atom, which has an atomic size close to that of a carbon atom and a five-electron valence structure (sp^2 hybridization), is naturally suited to a 2D strong covalent network structure similar to that of graphene [9], which provides a basis for further research and rationalization of its application. In recent years, 2D-PANI, with its novel 2D carbon and nitrogen network structure, has not only contributed to an in-depth study of its physical and mechanical properties both experimentally and theoretically [10–13], but its heterostructures have also shown remarkable performance in thermal management and energy storage [14,15]. Specifically, it exhibits ultra-high elastic modulus and high temperature stability better than graphene in air. Meanwhile, experimental studies [10] have demonstrated that the bandgap tuning ($2.74 \sim 1.57eV$) of C_3N quantum dots by varying their size between $1.8nm$ and $5.5nm$. As a 2D tunable narrow bandgap semiconductor material with both ferromagnetic properties and potential applications for

* Corresponding author.
E-mail address: emqhan@scut.edu.cn (Q. Han).

https://doi.org/10.1016/j.ijheatmasstransfer.2021.121235
0017-9310/

optoelectronic devices, 2D-PANI is expected to stand out in the post-silicon electronics industry.

Further, whether considering the heat dissipation of components in the microelectronics industry or the critical thermoelectric quality factor in thermal functional devices, it is certainly significant to clarify the thermal transport properties of 2D-PANI. The reality is that the implementation of accurate experimental measurements of the thermal conductivity of 2D materials still has great obstacles in technology and cost, so theoretical and simulation studies are effective technical tools that can provide some guidance for further research. In a theoretical study, starting from the Boltzmann transport equation (BTE) approach based on first principles, Kumar et al. [16] reported an ultra-low lattice thermal conductivity of $\sim 128 Wm^{-1}K^{-1}$ for pristine 2D-PANI. In a related study, Peng et al. [17] took the same approach to give results for $\sim 482 Wm^{-1}K^{-1}$, and it is clear that there is a gap between the two. In terms of molecular dynamics (MD) simulation studies, Mortazavi et al. [8] reported the thermal conductivity of pristine 2D-PANI at room temperature by an infinite extrapolation method based on non-equilibrium molecular dynamics (NEMD) of $815 \pm 20 Wm^{-1}K^{-1}$, which is between that of monolayer hexagonal boron nitride (h-BN) ($\sim 656 Wm^{-1}K^{-1}$) and graphene ($\sim 2460 Wm^{-1}K^{-1}$) [18,19]. The reproducibility of the results of this study is reflected in the fact that other similar MD studies have produced results of around $800 Wm^{-1}K^{-1}$ [20–22], using the same method and the potential function. In particular, Dong et al. [20] obtained thermal conductivity results in the case of taking the ReaxFF force field to describe the C-C interaction in 2D-PANI as $\sim 462 Wm^{-1}K^{-1}$. Unfortunately, the predictions of thermal conductivity based on the BTE and MD methods apparently fail to show good agreement, which may be due to differences in the description of phonon interactions. Thus, there are still many unknowns and uncertainties regarding to phonon transport and its thermal conductivity in 2D-PANI, which remains an interesting challenge.

It is important to note here that the MD simulations mentioned above were all done under the open source software, Large Scale Atomic/Molecular Massively Parallel Simulator (LAMMPS) [23]. However, the per-atom stress-based heat current expression used by LAMMPS works well for two-body potential systems, but not for multi-body potential cases such as the Tersoff potential describing 2D-PANI interatomic interactions [24–26]. This fundamental mistake causes the calculated predictions to be a gross underestimate of the actual thermal conductivity of the material, which has occurred in both graphene and h-BN calculations [18,19]. It makes the thermal conductivity results of 2D-PANI, which is inconclusive, even more confusing. With this issue surfacing, a rational re-evaluation of the thermal conductivity of 2D-PANI must be imminent. In addition, structural defects are often unavoidable in the preparation of micro-nano-scale materials, especially 2D materials with a mono-atomic thickness. On the other hand, defect engineering in which defects are selectively and artificially introduced through appropriate techniques (e.g. ion beam irradiation and focal electron) to modulate their physicochemical properties also has promising applications [27,28]. Therefore, it is also important and urgent to explore the effects of different defects on the thermal conductivity of 2D-PANI by means of a correct and suitable simulation method, which has guiding significance for defect engineering in 2D-PANI.

In the current study, extensive large-scale MD simulations were performed to explore the thermal transport properties of pristine and defective 2D-PANI, which reflected by their thermal conductivities. Firstly, the thermal conductivity of pristine 2D-PANI at room temperature was calculated by homogeneous non-equilibrium molecular dynamics (HNEMD) [29], equilibrium molecular dynamics (EMD) [30,31], and spectral heat current decomposition (SHC) [32–34] methods, respectively. Each of the three methods plays its own strengths against the same object and acts as a cross-check on the computational results to improve its reliability. Next, the effects of three structural defects, monovacancy, divacancy, and Stone-wales, and their concentrations on the thermal conductivity of 2D-PANI were explored by the HNEMD method. A specific comparison and analysis of the phonon density of states (PDOS) in the frequency domain and the phonon participation rate (PPR), which reflects the phonon localization characteristics, were carried out in order to reveal the specific mechanism of the influence of various defects on the thermal transport of 2D-PANI. Last, as a key factor affecting the lattice vibration, the effect of temperature on the thermal conductivity of 2D-PANI has also been investigated.

2. Models and methods

2.1. Models for 2D-PANI

The 2D-PANI atomic configuration in this study is shown in Figs. 1(a-b), which exhibits a hexagonal honeycomb lattice structure similar to the graphene. Structurally, it can be approximated as the product of the regular substitution of nitrogen atoms for some of the carbon atoms in graphene. On this basis, three structural defects commonly found in 2D materials [18,19], monovacancy, divacancy, and Stone-Wales (SW), are introduced respectively, constituting three defective 2D-PANIs, as shown in Figs. 1(c-e). For ease of understanding, we next refer to the atom in the structure that change when introducing defects as the "core atom".

The first type is the vacancy defects containing both monovacancy and divacancy defects. The former is formed by the absence of a single atom, while the latter implies a situation where two neighboring atoms are missing at the same time. Due to the structural peculiarities of 2D-PANI, the monovacancy defects considered in this study includes four possible cases, which are determined by a combination of two core atom types and two modes of orientation. In contrast, the divacancy defects contain a total of six possible configurations, which are determined by the fact that there are three different orientations for each of the two core atom combinations, C-C and C-N. It should be noted that the three orientations here correspond to three different chemical bond orientations in the hexagonal ring structure. To be more precisely, the vacancy here refers to the category of the structural defect at the time of its initial construction. With the structural random fluctuations in the thermal equilibrium process, more complicated atomic rings will be formed at the vacancy defects to tend towards a lower energy steady state, such as the pentagons in the monovacancy and the 5-8-5 atomic configuration in the divacancy. The second type is the topological defect represented by SW defects, which are widely found in 2D materials such as graphene and are constructed by in-plane 90° rotation of a chemical bond and its bonding atoms. Due to the consistency in core atoms and the orientation modes, the possible configurations for SW defects are the same as the divacancy defects described above, as shown in Figs. 1(d-e).

In the process of introducing defects, the randomness of their distribution specifically includes two aspects: randomness of position and randomness of orientation. By considering both of the two aspects of randomly constructed defects, the potential influence of the specificity of the defective sample on its thermal transport properties can be effectively avoided. Further, the defects concentration is defined as the ratio of the number of non-hexagonal rings in the defective sample to the number of hexagonal rings in the pristine sample with the same size. To this end, special algorithms have been developed in this study for the construction of 2D-PANI models of randomly distributed defects with the above specified defect types and concentrations.

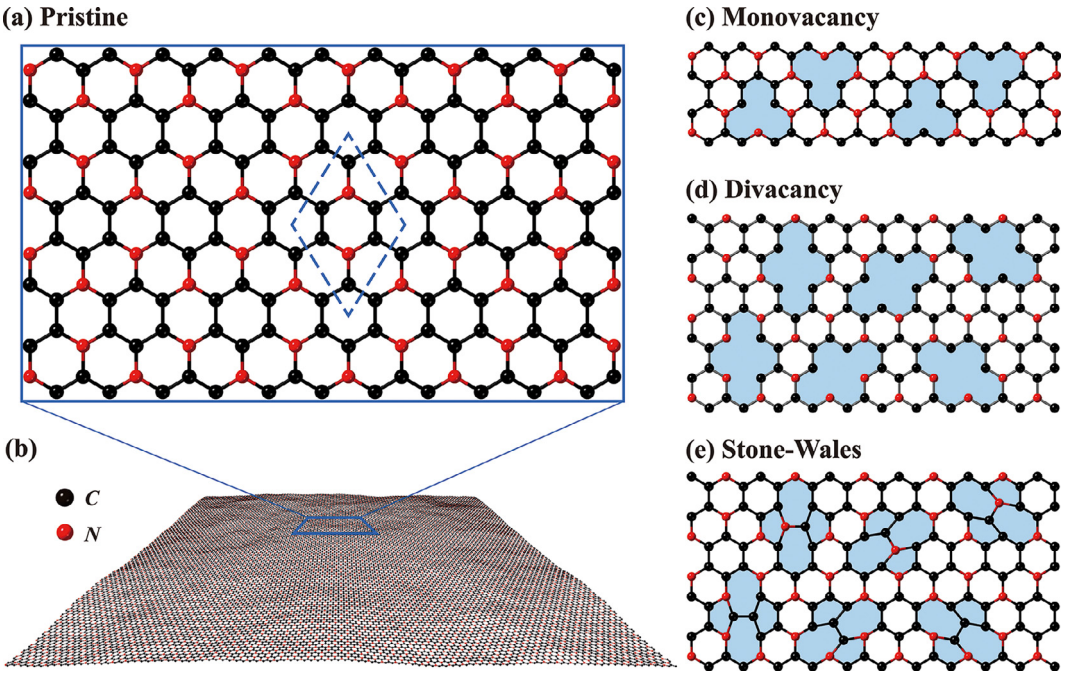

Fig. 1. (a) Schematic illustration of the atomic model for the pristine 2D-PANI, where the dashed box contains the cell unit; (b) Perspective view of the pristine 2D-PANI with an in-plane dimension of $25nm \times 25nm$ after equilibration at 300K, to illustrate the structure; (c) Schematic diagram of the four monovacancy defects containing two different orientations and two different core atoms (C and N atoms); Schematic diagram of six divacancy (d) and SW (e) defects containing three different orientations and two different combinations of core atoms (C-C and C-N), respectively. (This defects schematic is only intended to describe how the defects are formed and their initial form. After thermal equilibrium, other complex defect structures, such as octagons, may also appear in the case of vacancy defects due to factors such as structural fluctuations.)

2.2. MD methods for thermal conductivity calculation

2.2.1. The HNEMD method

In 1982, based on non-canonical linear response theory, Evans [29] proposed the homogeneous non-equilibrium molecular dynamics (HNEMD) method, which cleverly reduces the thermal transport problem to a mechanical analog to achieve the calculation of thermal conductivity. Specifically, it simulates the effects of thermal gradient by applying a suitable fictitious force field in a fixed direction to the system and achieves the calculation of thermal conductivity through the linear response of the virial heat current vector relative to the fictitious force field. The homogeneity of this method is reflected in the fact that no real temperature gradient is generated in the system, and the external force applied to simulate the temperature gradient reflect its non-equilibrium nature. In 2009, Mandadapu et al. [35] extended the original HNEMD method from being used only for the two-body potential system to a special class of multi-body potential systems that can be used for the cluster potential. A decade later, Fan et al. [34] further extended it to be applicable to universal multi-body potential systems, including the Tersoff potential in this study.

In this method, the key external driving force, $\vec{F}_i^e$, acting on the atom i and used to generate the homogeneous heat current is:

$$\vec{F}_i^e = \sum_{j \neq i} \left(\frac{\partial U_j}{\partial \vec{r}_{ji}} \otimes \vec{r}_{ij} \right) \cdot \vec{F}_e \tag{1}$$

where U_j is the potential of the atom j, $\vec{r}_{ij}$ and $\vec{r}_{ji}$ are the position vectors between atom i and j, and $\vec{F}_e$ is the vector parameter controlling the direction and magnitude of the external driving force.

Thus, in a multi-body potential system, the total force $\vec{F}_i^{tot}$ on atom i is the sum of the external driving forces described above and the inter-atomic forces inherent in the system:

$$\vec{F}_i^{tot} = \vec{F}_i^i + \vec{F}_i^e = \sum_{j \neq i} \left[\frac{\partial U_i}{\partial \vec{r}_{ij}} - \frac{\partial U_j}{\partial \vec{r}_{ji}} + \left(\frac{\partial U_j}{\partial \vec{r}_{ji}} \otimes \vec{r}_{ij} \right) \cdot \vec{F}_e \right] \tag{2}$$

where $\vec{F}_i^i$ represents the inter-atomic force on the atom i, that is, the internal force term.

Under the effect of the external force, the system will be heated up so that the system temperature deviates from the preset temperature. Therefore, while the thermostat keeps the system temperature constant, the following correction values C are further introduced in order to maintain the total system momentum:

$$\vec{F}_i^{tot} \to \vec{F}_i^{tot} - C = \vec{F}_i^{tot} - \frac{1}{N} \sum_i \vec{F}_i^{tot} \tag{3}$$

Further, for a general multi-body potential system, the heat current equation can be described as:

$$\vec{Q} = \sum_{i.j \neq i} \vec{r}_{ij} \left(\frac{\partial U_j}{\partial \vec{r}_{ji}} \cdot \vec{v}_i \right) \tag{4}$$

Note that only the potential energy term of the heat current vector is considered here and the kinetic term, which makes little contribution to the thermal conductivity of the solid, is ignored [35]. The thermal conductivity with time in a given direction is:

$$\kappa(t) = \frac{\langle \vec{Q}(t) \rangle_{ne}}{TV \left| \vec{F}_e \right|} \tag{5}$$

Where $\langle\rangle_{ne}$ denotes the non-equilibrium ensemble average, that is, the time average in the MD simulation. T and V denote the temperature and volume at which the system is located, respectively. For 2D-PANI, the volume is generally considered to be the product of the surface area and thickness, which is $0.32nm$ [8]. And its lattice constant is about $0.48nm$. $\left| \vec{F}_e \right|$ denotes the modulus of the vector $\vec{F}_e$, that is, its numerical magnitude; for simplicity, F_e is used consistently to present it, and its dimension is the inverse length. Further, Eq. (5) is rewritten in a cumulative averaging manner to facilitate the observation of convergence and to obtain the

final thermal conductivity result:

$$\kappa(t) = \frac{1}{t}\int_0^t \frac{\langle \vec{Q}(\tau)\rangle_{ne}}{TVF_e} d\tau \tag{6}$$

A crucial issue in this method is the choice of the external driving force parameter F_e, which is critical to achieving a perfectly linear response and a sufficiently large signal-to-noise ratio. The rule-of-thumb [34–36] suggests that basically the conditions of $F_e\lambda \le 1/10$ or $F_e\lambda_{\max} \le 1$ should be satisfied, where λ and $\lambda_{\max}$ are the mean free path (MFP) of the characteristic phonons in the system and the maximum phonon MFP, respectively. In practical problems, a few F_e values with a large span can be predicted and tested to determine the appropriate parameters for further calculations.

Since distinct characteristics are expected for the in-plane and out-of-plane components in 2D materials, the in-out decomposition of the thermal conductivity was achieved by performing the following decomposition of the heat current in Eq. (4):

$$\begin{aligned}\vec{Q}_{in} &= \sum_{i,j\neq i} \vec{r}_{ij}\left(\frac{\partial U_j}{\partial x_{ji}}\vec{v}_{xi} + \frac{\partial U_j}{\partial y_{ji}}\vec{v}_{yi}\right)\\ \vec{Q}_{out} &= \sum_{i,j\neq i} \vec{r}_{ij}\left(\frac{\partial U_j}{\partial z_{ji}}\vec{v}_{zi}\right)\end{aligned} \tag{7}$$

Where the in-plane component is located in the xy plane and the out-of-plane component corresponds to the z direction. Analogous to this method, the in-out decomposition of thermal conductivity can also be applied to the following EMD and SHC methods.

2.2.2. The EMD method

Another common method used for lattice thermal conductivity calculations, the equilibrium molecular dynamics (EMD) method, is based on the Green-Kubo equation [30,31], which reflects the transport coefficient at nonequilibrium by the fluctuation of the corresponding physical quantities at equilibrium. In this method, the running lattice thermal conductivity tensor $\kappa_{\alpha\beta}(t)$ $(\alpha, \beta = x, y, z)$ can be expressed as an integral of the heat current auto-correlation function (HCACF) as:

$$\kappa_{\alpha\beta}(t) = \frac{1}{k_B T^2 V}\int_0^t \left\langle Q_\alpha(0) Q_\beta(t')\right\rangle_e dt' \tag{8}$$

Where k_B is the Boltzmann constant, T, V and Q have the same physical meaning as them described in Eqs. (4,5) previously. $\langle\rangle_e$ denotes the ensemble average at equilibrium state, that is, the average result of the physical quantities in angle brackets at different time points. For a 2D material lying in the xy plane, the possible anisotropy of the thermal conductivity in this plane is not taken into account. And since the thermal conductivity tensor is diagonal, this scalar thermal conductivity can be expressed as the final result:

$$\kappa = \frac{1}{2}(\kappa_{xx} + \kappa_{yy}) \tag{9}$$

It should be noted that the signal-to-noise ratio of the HCACF calculated in the EMD method decreases as the correlation time increases, but only a sufficiently long correlation time will give stable results. Therefore, for each set of calculation, several independent simulations need to be carried out, and the results are averaged to obtain a stable running thermal conductivity value.

2.2.3. The spectral heat current decomposition method

The spectral heat current (SHC) decomposition method [32–34], based on the determination of the spectral decomposition of the heat current by a dynamic correlation function obtained from non-equilibrium MD simulations, is used to calculate the frequency-dependent thermal conductivity of the material. Initially, the method was used to study the frequency-dependent contribution of inelastic scattering to the thermal conductivity of interfaces based on non-equilibrium steady states established by non-equilibrium molecular dynamics (NEMD-based SHC) [32]. Later, Fan et al. [34] further extended the method to HNEMD and proposed the HNEMD-based SHC method. The former corresponds to the quasi-ballistic transport phase for finite systems, while the latter targets transport coefficients for infinite systems, and the two can be combined and extrapolated to achieve predictions of length-dependent thermal conductivity results.

First, a force-velocity correlation function in the non-equilibrium steady-state needs to be defined:

$$\vec{K}(t) = \sum_i \sum_{j\neq i} \left\langle \left[\vec{W}_j(0)\cdot\vec{v}_i(t)\right]\right\rangle_{ne} \tag{10}$$

where the virial force of the atom j is $\vec{W}_j = \vec{r}_{ij}\cdot(\partial U_j/\partial \vec{r}_{ji})$, the velocity $\vec{v}_i$ of atom i and the momentum $\vec{p}_i$ have the following relationship: $\vec{v}_i = \vec{p}_i/m_i$.

Further, the Fourier transform and its inverse transform are performed on the above steady-state correlation function:

$$\tilde{\vec{K}}(\omega) = \int_{-\infty}^{+\infty} e^{i\omega t}\vec{K}(t)dt \quad , \quad \vec{K}(t) = \int_{-\infty}^{+\infty} e^{-i\omega t}\vec{K}(\omega)\frac{d\omega}{2\pi} \tag{11}$$

When $t = 0$, Eq. (10) agrees with the potential energy term of the non-equilibrium heat current, i.e. Eq. (5). At the same time using the definition of inverse transformation, we can get:

$$\begin{aligned}\vec{Q} \equiv \vec{K}(0) &= \int_{-\infty}^{+\infty} \tilde{\vec{K}}(\omega)\frac{d\omega}{2\pi}\\ &= \int_0^{+\infty}\left[2\tilde{\vec{K}}(\omega)\right]\frac{d\omega}{2\pi}\\ &= \int_0^{+\infty} q(\omega)\frac{d\omega}{2\pi}\end{aligned} \tag{12}$$

The spectral decomposition of the heat current can thus be obtained in the form of:

$$q(\omega) = 2\tilde{\vec{K}}(\omega) \tag{13}$$

For the NEMD and HNEMD methods, both can achieve a non-equilibrium steady-state with non-zero heat current during the simulation. The SHC calculations based on the NEMD and HNEMD methods give the spectral thermal conductance $G(\omega)$ and spectral thermal conductivity $\kappa(\omega)$, respectively:

$$G(\omega) = \frac{q(\omega)}{V\cdot\Delta T} \quad , \quad \kappa(\omega) = \frac{q(\omega)}{TVF_e} \tag{14}$$

where ΔT is the temperature difference between the heat source and the heat sink that generates the heat current in the NEMD method and the other physical quantities have the same meaning as previously described.

In an infinite system, the phonon MFP is defined by the ratio of the thermal conductivity κ under diffusive transport to the thermal conductance G under ballistic transport [37], and is generalized in the frequency domain as follows:

$$\lambda = \frac{\kappa}{G} \quad , \quad \lambda(\omega) = \frac{\kappa(\omega)}{G(\omega)} \tag{15}$$

Also, the frequency dependence of the length-dependent thermal conductivity obtained from the following classical first-order extrapolation formula [38] is further considered:

$$\frac{1}{\kappa(L)} = \frac{1}{\kappa}\left(1 + \frac{\lambda}{L}\right) \quad , \quad \frac{1}{\kappa(\omega, L)} = \frac{1}{\kappa(\omega)}\left(1 + \frac{\lambda(\omega)}{L}\right) \tag{16}$$

Finally, the length-dependent thermal conductivity $\kappa(L)$ can be obtained by integrating the $\kappa(\omega, L)$ in Eq. (16) in the frequency domain:

$$\kappa(L) = \int_0^\infty \kappa(\omega, L)\frac{d\omega}{2\pi} \tag{17}$$

2.2.4. Details of the MD simulations

All MD simulations in this paper were implemented by the efficient graphics processing units molecular dynamics (GPUMD) code [24,39,40], which provides a generalized force algorithm for multi-body potentials to achieve accurate heat current formulations applicable to multi-body potential systems. It not only effectively solves the problem of LAMMPS in calculating the heat current formula of the multi-body potential system [18,19,24], but also greatly saves the calculation cost by taking full advantage of the computational performance of the GPU architecture. For the C-C and C-N inter-atomic interactions present in 2D-PANI, they were described by the optimized Tersoff potential functions developed by Lindsay et al. [41] and Kınacı et al. [35], respectively, which were also widely used in several previous studies [42–44]. The former provides a better fit to experimental data for phonon dispersion data for graphene containing C-C bonds than the original Tersoff potential, while the latter reproduces the ab initio energetics for C-N bonds. In addition, a time step of $1fs$ was chosen throughout the simulations, which is small enough to ensure good system stability and energy convergence.

For all simulations in this study the same equilibrium process was used, that is, 10 million time steps ($1ns$) at the corresponding temperature conditions using the NPT ensemble controlled by the Berendsen thermostat. Next, according to the different MD methods, the thermostats were switched, the ensembles were changed and the respective calculation and output processes were carried out. Further, the data produced under each method was post-processed and visualized, which will be described in detail later on.

3. Results and discussion

3.1. Thermal conductivity of pristine 2D-PANI

In this section, the thermal conductivity of the infinite pristine 2D-PANI at 300K was calculated by three methods: HNEMD, EMD, and SHC. The results obtained from the three methods were compared and cross-checked with each other, while taking advantage of the unique strengths of each in order to gain some new insights and understanding of the thermal conductivity of 2D-PANI.

3.1.1. Results from HNEMD simulations

The calculation of the thermal conductivity of the pristine 2D-PANI was completed by the HNEMD method, while the simulation details and size-dependent effects under this method were meaningfully explored. For each independent simulation, the system was equilibrated and then switched to the NVT ensemble with the Nosé-Hoover thermostat to maintain the overall temperature around the target temperature. Next, according to the specific value of F_e, calculations of up to $10ns$ (10 million time steps) were performed in both of the x and y directions within the in-plane of 2D-PANI. Throughout the simulation, periodic boundary conditions were adopted in both directions in the in-plane and free boundary conditions were adopted in the out-of-plane direction, so that the result were calculated as the thermal conductivity value of an infinite sample. Ignoring the possible anisotropy and taking the overall lattice thermal conductivity of the material as the main consideration, the average of the thermal conductivity in the two directions in the in-plane was taken as the thermal conductivity result. And in the following visualizations, each resultant curve is an average of the thermal conductivity in both directions in the in-plane.

First, the thermal conductivity of 2D-PANI was calculated and the details of the simulation in HNEMD were discussed. At a temperature of 300K, 2D-PANI with an in-plane size of $25nm \times 25nm$ was selected as the object of thermal conductivity calculation, which contains 24,000 atoms. As emphasized in 2.2.1, in the HNEMD method, the selection of external driving force parameters F_e is critical. Referring to the selection of driving force parameters in the HNEMD method applied to Gr [34] and h-BN [18], tests were carried out under seven different values of $0.05\mu m^{-1}$, $0.1\mu m^{-1}$, $0.2\mu m^{-1}$, $0.4\mu m^{-1}$, $0.6\mu m^{-1}$, $0.8\mu m^{-1}$, and $1.0\mu m^{-1}$ respectively. During the parameter testing, it is the convergence of the thermal conductivity calculations with simulation time that requires attention, not the specific value of the results. At the same time, in order to show the convergence more clearly, only one independent simulation in each of the two in-plane directions was carried out for each different value, and the final result was averaged and shown in Figs. 2(a-b). From the visualization results, it is not difficult to find that in the cases of the test value of $F_e \geq 0.2\mu m^{-1}$, the thermal conductivity calculation results of the 2D-PANI based on HNEMD were divergent over time. As a comparison, its convergence over time is good at $F_e = 0.05\mu m^{-1}, 0.1\mu m^{-1}$. In particular, the thermal conductivity result converged from $5ns$ onwards and the curve smoothed out, indicating that the linear-response regime is well achieved. In this way, the finalization of the driving force parameter F_e in the HNEMD method has been completed, and since then, $F_e = 0.1\mu m^{-1}$ was chosen for all subsequent simulations based on this method. Furthermore, for subsequent samples with defects, the values of the driving force parameter will be still sufficient to meet the rule-of-thumb in the case of reduced phonon MFP.

Next, two independent sets of HNEMD simulations were performed on the above model, each of which includes two simulations in both directions, and the thermal conductivity results are shown in Fig. 2(d). For each independent simulation, the running thermal conductivity obtained by Eq. (5) has large fluctuations as shown by the thin line in Fig. 2(c), which is extremely detrimental to the assessment of the convergence of the results. The thermal conductivity results redefined by Eq. (6) converge well with increasing time, owing to the time average in the MD simulation to represent the non-equilibrium ensemble average. Observing the results of the two independent simulations represented by the thin lines in Fig. 2(d), it is not difficult to find that as the simulation time increases, the deviation between the two becomes smaller. Especially after $5ns$, the two thin lines representing the results of two independent simulations will become difficult to distinguish. In this way, it is shown that two independent sets of simulations are sufficient to avoid spurious effects associated with a particular choice of initial velocity.

Then, for the running thermal conductivity average shown in Fig. 2(d) after the above processing, it will undergo the following post-processing process to obtain the final thermal conductivity calculation results. Since the non-equilibrium heat current in this method was directly calculated with a constant signal-to-noise ratio, the average result (represented by the thick line) over $5 \sim 10ns$ can be averaged in 100 small pieces and treated them as independent results. Statistical averaging of these independent results and calculation of the standard deviation gives a thermal conductivity value of $2013 \pm 23 W m^{-1} K^{-1}$ for the pristine 2D-PANI at 300K. In addition, for 2D materials, the existence of their special flexural phonon mode, that is, the out-of-plane part of the phonon mode, creates extraordinary phonon dynamics. In-out decomposition of thermal conductivity can be achieved by a corresponding decomposition of heat current, which will undoubtedly drive deeper insights into thermal transport in 2D materials. As shown in Fig. 2(d), the out-of-plane component of the thermal conductivity of 2D-PANI accounts for about two-thirds of its total thermal conductivity and is significantly higher than the in-plane component, which is similar to the calculated results of graphene [33].

In the above process, the selection of key parameters under the HNEMD method and the related description of data processing were completed. Next, another important issue in the calculation

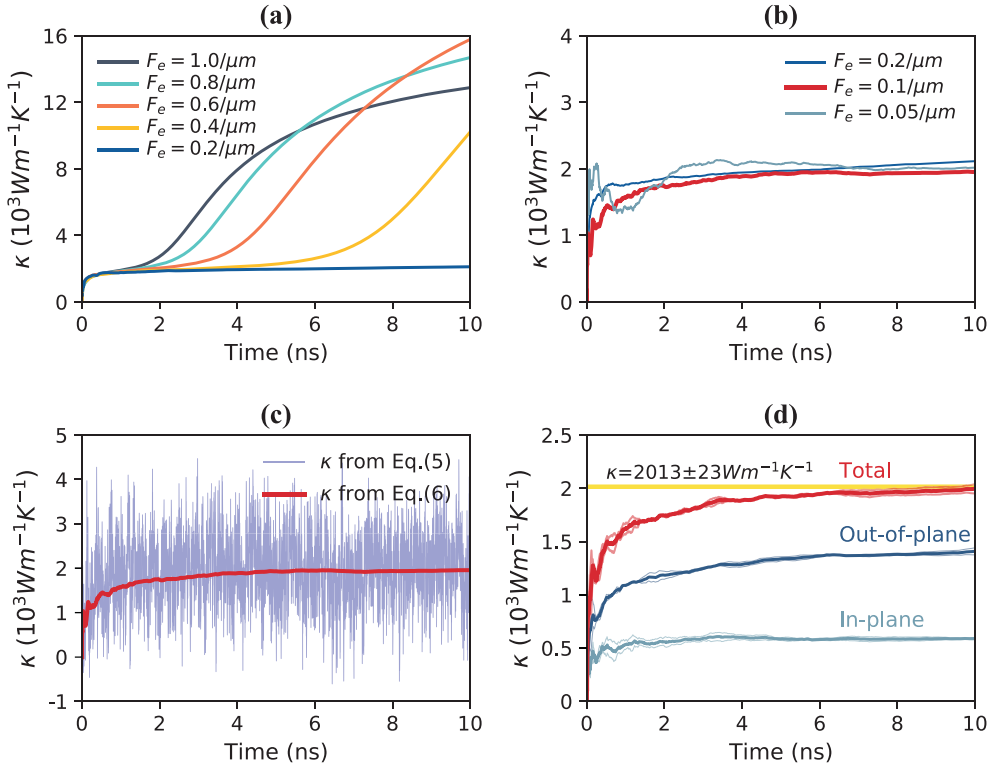

Fig. 2. At 300K, the process and results of calculating the thermal conductivity of the pristine 2D-PANI with the size of $25nm \times 25nm$ based on the HNEMD method. (a) Results of the 2D-PANI thermal conductivity when F_e took values from $0.2\mu m^{-1}$ to $1.0\mu m^{-1}$ and the interval was $0.2\mu m^{-1}$. (b) When the values of F_e were $0.05\mu m^{-1}$, $0.1\mu m^{-1}$, $0.2\mu m^{-1}$ respectively, the calculation results of the thermal conductivity of 2D-PANI. (c) When $F_e = 0.1\mu m^{-1}$, the processing of 2D-PANI thermal conductivity calculation results: the thin blue line represents the result obtained by Eq. (5), and the thick red line represents the result of cumulative average processing of the former by Eq. (6). (d) When $F_e = 0.1\mu m^{-1}$, the variation of the 2D-PANI running thermal conductivity with time based on the HNEMD method. Where the thin line indicates the results of the independent simulations and the thick line indicates the average of the results of the two sets of independent simulations. In addition, the total thermal conductivity (llabelled by "Total") is further decomposed into an in-plane component (labelled by "In-plane") and an out-of-plane component (labelled by "Out-of-plane"). The yellow area is the reference span for the thermal conductivity results to verify convergence.

of 2D-PANI thermal conductivity based on this method will be explored, which is also of considerable importance in thermal transport at the micro-nano-scale: the size-dependent effect. Five sets of pristine 2D-PANI samples of sizes $5nm \times 5nm$, $10nm \times 10nm$, $15nm \times 15nm$, $25nm \times 25nm$, and $50nm \times 50nm$ were selected for the calculation, with atomic numbers of 960, 3840, 8640, 24000, and 96000, respectively. Due to the differences in size of the samples, the data output processing needs to be adjusted to facilitate comparison and analysis among groups. The number of independent simulations performed on the above samples was 10, 8, 4, 2,and 1, where each set also contained two simulations both in the x and y directions; the time intervals for the thermal conductivity results were $1.0ns$, $0.8ns$, $0.4ns$, $0.2ns$, and $0.1ns$, respectively. At the same time, the total duration of each group of independent simulations is set to $15ns$, where the data produced within $5ns \sim 15ns$ was used for statistical and computational purposes. As a result, 100 independent thermal conductivity calculations can be output for each size, and these results were further visualized as frequency histograms, as shown in Figs. 3 (a-e).

Overall, the results of the 2D-PANI thermal conductivity based on the HNEMD method showed a clear size-dependent effect. When the size of sample was relatively small, the thermal conductivity values were spread over a wide range and the results were too dispersed to achieve the desired statistical accuracy. At the same time, the insufficient out-of-plane deformation in the relatively small simulated samples leads to an underestimation of phonon scattering caused by the acoustic flexural modes and consequently to an overestimation of their thermal conductivity results, which has a precedent in the calculation of graphene [45,46]. And when the simulated system is expanded to $25nm \times 25nm$, the distribution of thermal conductivity values was concentrated, showing good statistical accuracy. The good convergence of the thermal conductivity results with respect to the number of atoms, which is proportional to the size of samples, was further clearly presented in Fig. 3(f). This is due to the mutual compensation between the boosting effect on the thermal conductivity of more long-wave phonons involved in transport and the weakening effect on the thermal conductivity of stronger phonon scattering as the size of sample increases. And then, the thermal conductivity showed a gradual decrease and convergence as the size of the sample increases. Thus, under the HNEMD method, a 2D-PANI with the size of $25nm \times 25nm$ containing 24,000 atoms can be used to obtain thermal conductivity results with the desired statistical accuracy in a feasible simulation time, which is a good choice for both computational accuracy and cost. This provides also guidance on the choice of the size of samples for the later stages of the process of calculating thermal conductivity based on the HNEMD method.

3.1.2. Results from EMD simulations

In order to cross-check the thermal conductivity results based on the HNEMD method described above, the corresponding calculations based on the EMD method were performed for the pristine 2D-PANI with the size of $25nm \times 25nm$ in this section. After completion of the equilibrium process, the sample was simulated 100 times independently by varying the initial velocity of the atoms, where each set of independent simulations was relevant for up to

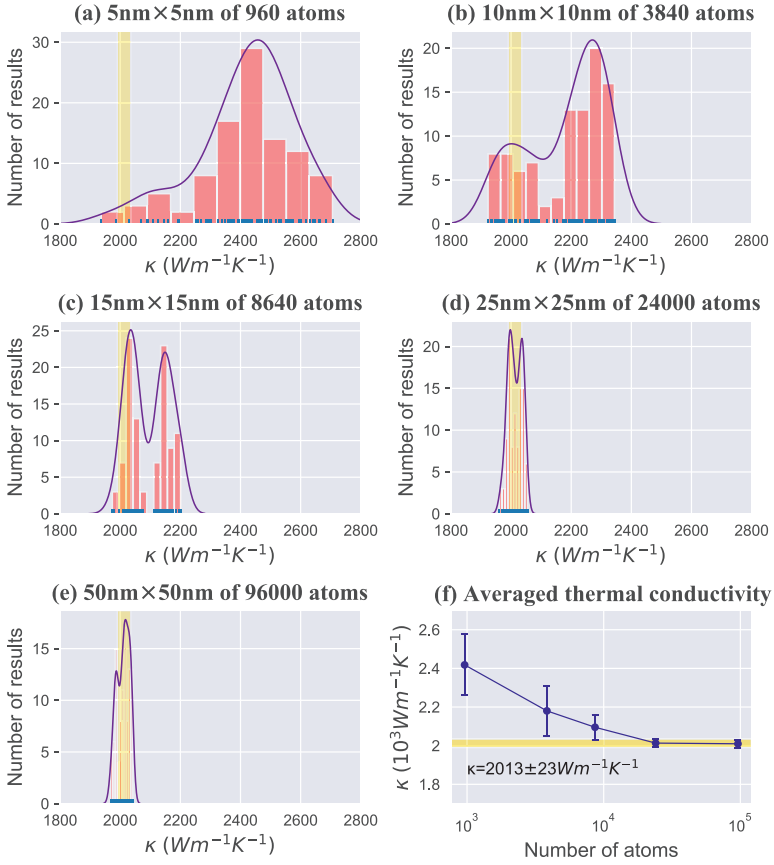

Fig. 3. (a-e) The distribution of the calculated thermal conductivity values for the pristine 2D-PANI with the size of $5nm \times 5nm$, $10nm \times 10nm$, $15nm \times 15nm$, $25nm \times 25nm$ and, $50nm \times 50nm$, respectively. Under the HNEMD method, where 100 thermal conductivity values are included for each simulated size. The kernel density estimate (KDE) results are plotted by the blue line, which gives a clear visual representation of the distribution of the thermal conductivity results by simulating the true probability distribution of the histogram data. The yellow part corresponds to the region with thermal conductivity of $2013 \pm 23 Wm^{-1}K^{-1}$. (f) Averaged thermal conductivity results versus the number of atoms in the simulated system, where the error bars were determined by the standard deviation of the respective 100 thermal conductivity values.

$10ns$. In fact, a good convergence of the average results for the running thermal conductivity was achieved when the correlation time reaches $1.5ns$, with the result of $1962 \pm 53 Wm^{-1}K^{-1}$. Therefore, in order to present the convergence process of the running thermal conductivity results more clearly, only the part of the correlation time of $0 \sim 1.5ns$ was shown in the visualization of the results in Fig. 4.

For the same pristine 2D-PANI samples, the thermal conductivity calculations based on the HNEMD and EMD methods were $2013 \pm 23 Wm^{-1}K^{-1}$ and $1962 \pm 53 Wm^{-1}K^{-1}$, respectively, which were in good agreement. At the same time, the in-plane and out-of-plane decomposition results for thermal conductivity under the EMD method were also in good agreement with the results under HNEMD in Fig. 2, as can be seen from the inset of Fig. 4. However, the total time spent in the output phase of the HNEMD method was only $40ns$, while the EMD method was up to $1000ns$, which is a significant difference. This is due to the fact that the signal-to-noise ratio of the HCACF in the EMD method decreases with increasing correlation time, which requires that the simulation be repeated as many times as possible to obtain more stable thermal conductivity results. The HNEMD method benefits from a sufficiently large signal-to-noise ratio due to an appropriate external driving force to obtain convergent thermal conductivity results with the desired statistical accuracy with a small number of iterations of the simulation. In this way, the HNEMD method showed a very high efficiency compared to EMD in terms of thermal conductivity calculations, which can lead to significant savings in calculation costs.

3.1.3. Results from spectral decomposition simulations

Spectral decomposition methods that enable spectral ballistic thermal conductance and spectral thermal conductivity calculations by spectral decomposition of the heat current have been successfully used for carbon nanotubes and graphene calculations [34]. Based on this method, while extrapolating the thermal conductivity of the material to the corresponding macroscopic dimensions, a large amount of frequency-dependent information such as phonon MFP can be also obtained, which facilitates further understanding of the phonon heat transport mechanisms involved.

As shown in Fig. 5(a) for the spectral thermal conductivity $\kappa(\omega)$ by the HNEMD-based SHC, the thermal conductivity contribution of 2D-PANI is mainly from out-of-plane phonon modes at frequencies less than $30THz$ and mainly in the lower frequency bands of $0-10THz$ and $20-30THz$. Combined with the NEMD-based SHC calculation of the spectral ballistic thermal conductance $G(\omega)$, the spectral phonon MFP $\lambda(\omega)$ information was further obtained by Eq. (15), as shown in Figs. 5(b-c). The spectral phonon MFP results indicated that 2D-PANI satisfies the $\lambda_{max} \approx 7000nm$ at 300 K. This quantitatively indicated that the external driving force in HNEMD calculations should roughly satisfy the condition of $F_e \leq 0.14\mu m^{-1}$, otherwise the thermal conductivity calculation results will be difficult to converge. This result matched perfectly with the actual test results in Figs. 2(a-b) and further quantitatively validated the reasonableness of the external driving force $F_e = 0.1\mu m^{-1}$ taken in this study. Furthermore, the length-dependent thermal conductivity results for 2D-PANI by first-order classical extrapolation of Eqs. (16,17) showed that it converges completely to around

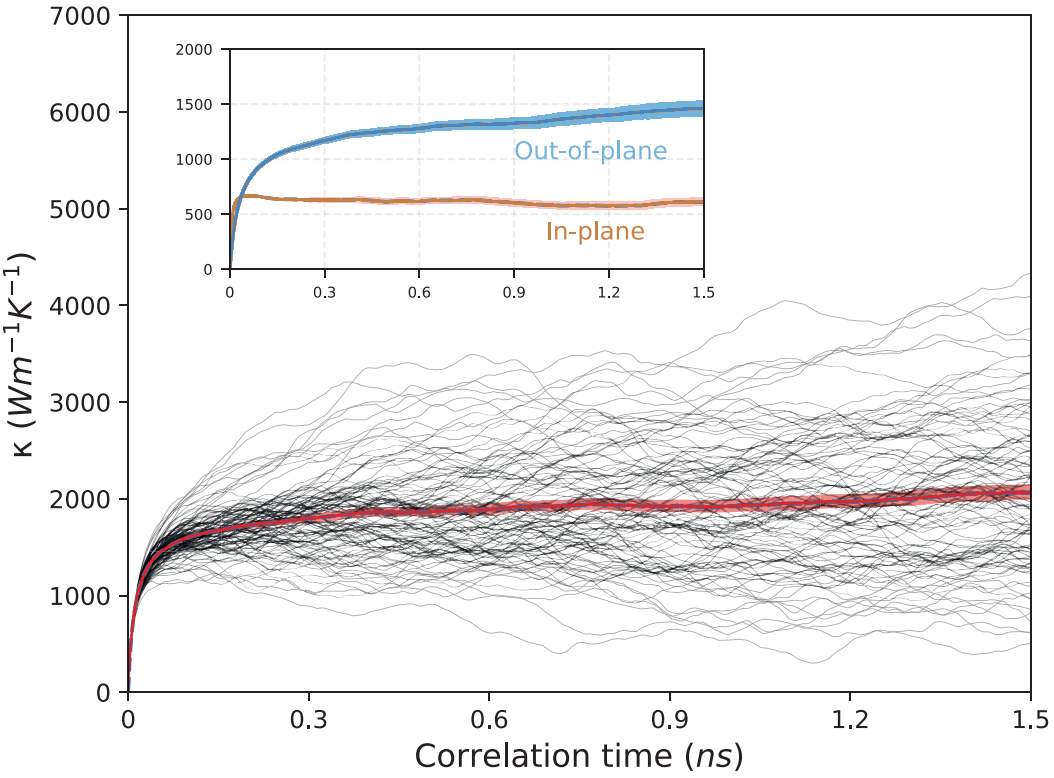

Fig. 4. Relationship between running thermal conductivity and correlation time at 300 K for a pristine 2D-PANI with the size of $25nm \times 25nm$ based on the EMD method. The thin black lines show the results of 100 independent simulations, while the thick red line and shaded area show the average results and their corresponding standard errors, respectively. The inset shows the average results for the in-plane and out-of-plane components of thermal conductivity as a function of the correlation time, and the shaded areas are the standard errors of the results of 100 independent simulations.

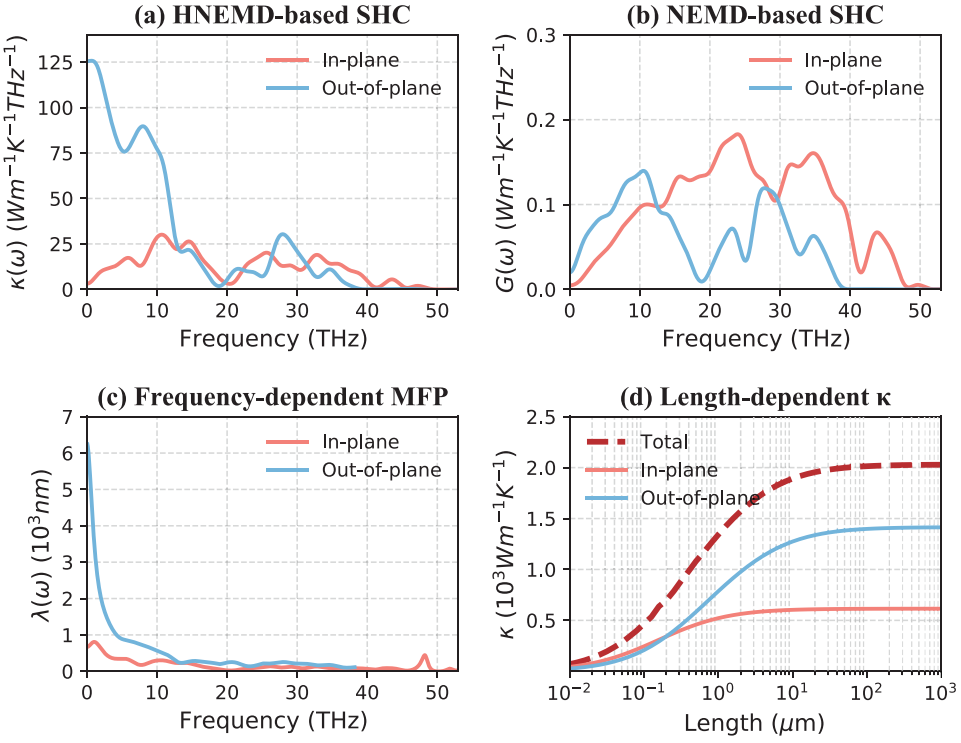

Fig. 5. The (a) spectral thermal conductivity $\kappa(\omega)$ and (b) spectral ballistic thermal conductance $G(\omega)$ and their (c) phonon mean free path $\lambda(\omega)$ results obtained from the HNEMD and NEMD based heat current spectral decomposition methods of pristine 2D-PANI at 300 K as a function of phonon frequency. (d) Calculation results of length-dependent thermal conductivity. For each of these four results an in-out decomposition was carried out to further clarify the respective contributions.

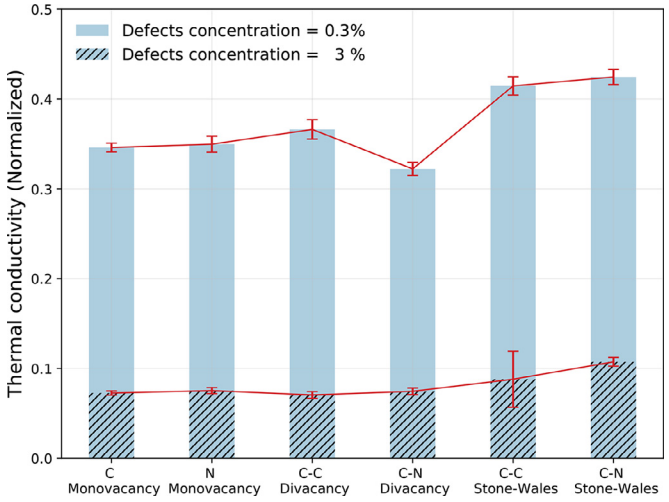

Fig. 6. Effect of defect type and its specific structure on the normalized thermal conductivity of 2D-PANI at 300 K for defects concentrations of 0.3% and 3% respectively. The normalized value of thermal conductivity is with respect to the value of pristine 2D-PANI at 300K. The error bar was represented by the standard deviation of the thermal conductivity calculation results of three samples with different random distribution defects.

$2023 W m^{-1} K^{-1}$ as the length approaches $1 mm$, which also agrees perfectly with the results of the previous two methods. Also, the in-plane and out-of-plane contributions to the thermal conductivity profile remained largely consistent with the HNEMD and EMD results as well. However, this calculation result is significantly higher than the other MD simulation results of approximately $800 W m^{-1} K^{-1}$ after length extrapolation, which may be the underestimation of the thermal conductivity caused by the error of LAMMPS, as mentioned before [20–22].

3.2. Thermal conductivity of defective 2D-PANI

3.2.1. Effect of defects

In this section, three types of structural defect with different concentrations of monovacancy, divacancy and SW were introduced into the pristine 2D-PANI with the size of $25 nm \times 25 nm$ at 300 K, as shown in Fig. 1, to explore the specific effects of the defects on their thermal conductivity. As 2D-PANI has a variety of defect configurations due to the specificity of its structure, the effect of each defect configuration on its thermal conductivity needs to be studied first. As shown in Figs. 1(c-e), the diversity of defect configuration modes was divided into C-vacancy and N-vacancy in monovacancy by the type of missing atom, and into C-C defects and C-N defects in terms of formation mode in divacancy and SW defects. For samples containing different defect configurations, the thermal conductivity of the sample was calculated for two defects concentrations of 0.3% and 3% to avoid additional effects of the defects concentration on the results. From the calculation results in Fig. 6, it is not difficult to find that for each type of defective 2D-PANI, the difference in the specific configuration of each defect had a negligible effect on the thermal conductivity result compared to the defects concentration and type. In addition, from the perspective of defect formation energy, in the case of each type of defect, the impact of the difference in the specific configuration is also very small [47,48]. Therefore, in the subsequent defective 2D-PANI thermal conductivity calculations, the differences caused by the specific configuration of each type of defect will be ignored, which is achieved by randomly assigning the specific configuration of the defect during its introduction.

The next step will be to explore the effect of three types of defect and their concentrations on the thermal conductivity of 2D-PANI in the following nine cases: 0.3%, 0.6%, 0.9%, 1.2%, 1.5%, 2.1%, 3%, 6% and 10%. In order to eliminate possible spurious effects due to the specific location of defects, three different samples were constructed for each case with a specific defect type and concentration by randomly assigning the specific location and configuration of the defects. Independent HNEMD simulations were performed for three samples at 300 K (details as described in 3.1.1) and the statistical average of these three results were used as the thermal conductivity result for a certain defective 2D-PANI with that concentration. With the superiority of the HNEMD method, the above approach allows the results to be more convincing while meeting the accuracy requirements of the calculation.

The overall results in Fig. 7 show that the defects caused a substantial weakening on the thermal conductivity of the 2D-PANI. Even small concentration of defects like 0.3% can reduce the thermal conductivity to less than half of its original value. This is due to the fact that the presence of defects destroys the original structural integrity, greatly enhancing phonon scattering and impeding effective heat transport processes. However, as the concentration of defects increased, the rate of decrease in thermal conductivity slowed down, especially after a defects concentration of more than 3%. This means that the weakening effect of structural defects on thermal conductivity at high concentrations almost saturates, which opens up more possibilities for defect engineering of structures and is instructive for their practical application. A longitudinal comparison of the results showed that the weakening effect of the SW defects on the thermal conductivity of 2D-PANI is significantly less than the other two defects with the same defects concentration. In particular, the thermal conductivity of defective 2D-PANI with monovacancy and divacancy defects at the same concentration were almost identical, as can be more visually presented in the logarithmic coordinate system of the inset in Fig. 7. Further, the normalized thermal conductivity results were fitted with low-power law related to the defects concentration, which can be equivalent to a linear fitting in a double logarithmic coordinate system. In order to verify the quality of the above fitting, calculations showed that all three achieve a goodness of fit with 0.98 or more, and their average is even close to 0.99. From the fitting results, the fitting functions for the thermal conductivity of the samples with monovacancy and divacancy defects were similar in power and significantly larger than those of the samples with SW defects, which allows a quantitative distinction to be made between the weakening effect of the three defects on the thermal conductivity of 2D-PANI.

Furthermore, compared with defective graphene, the influence of structural defects on the thermal conductivity of the two materials shows a strong consistency in both trend and magnitude, especially in the case of high defects concentrations. However, when the defects concentration is 0.3%, the normalized thermal conductivity of defective graphene is 0.45 ± 0.08 [19], which is significantly higher than the 0.37 ± 0.05 of defective 2D-PANI. This is due to that 2D-PANI can be regarded as graphene doped with periodic nitrogen atoms, which further strengthens the phonon anharmonicity caused by the defects to a certain extent. At high defect concentrations, the dominant effect of defects becomes more pronounced and gradually weakens the difference between the normalized thermal conductivity of the two as influenced by defects.

In addition, an in-out decomposition of the above thermal conductivity results has also been performed and their respective weightings were shown in Fig. 8. From the results in it, the percentage of thermal conductivity components in-plane and out-of-plane of the three defective 2D-PANIs were similar in trend with defects concentration and do not exhibit significant differences. In the pristine 2D-PANI, the in-plane component of the thermal conductivity was only about one-third of the total thermal conductivity, which has been validated against each other in the previ-

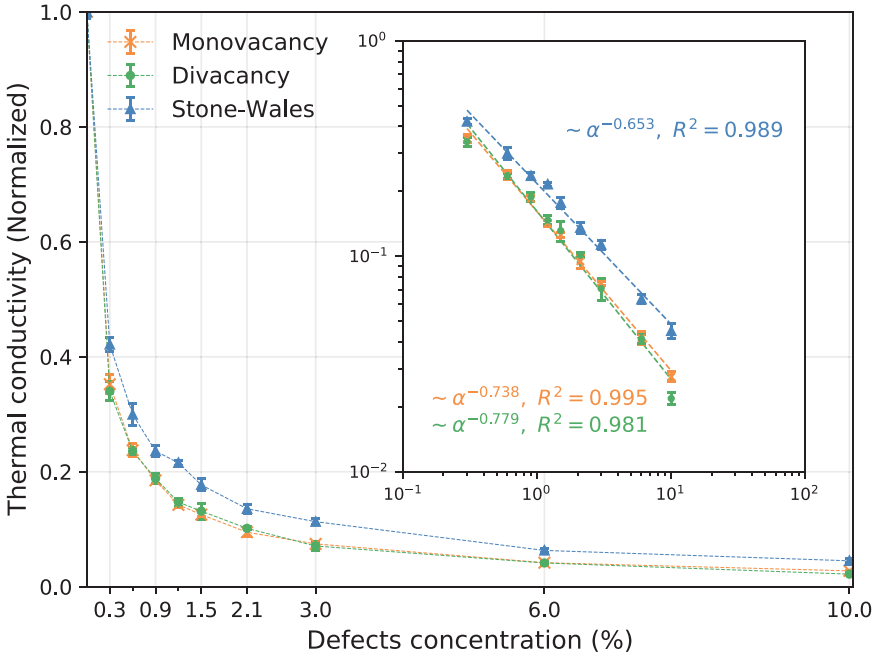

Fig. 7. Normalized thermal conductivity as a function of defects concentration for three types of defective 2D-PANI containing monovacancy, divacancy and SW at 300 K. The defects concentration contains nine cases of 0.3%, 0.6%, 0.9%, 1.2%, 1.5%, 2.1%, 3%, 6%, and 10%. The inset further presents the above relationships in double logarithmic coordinates and a low-power law fitting to the normalized thermal conductivity data with respect to the defects concentration α. Here, R^2 is a parameter that measures the overall goodness of the fitting function, and the closer it is to 1, the better the fitting is. The error bars of the thermal conductivity data were represented by the standard deviation of the results of three thermal conductivity calculations for samples with different randomly distributed defects.

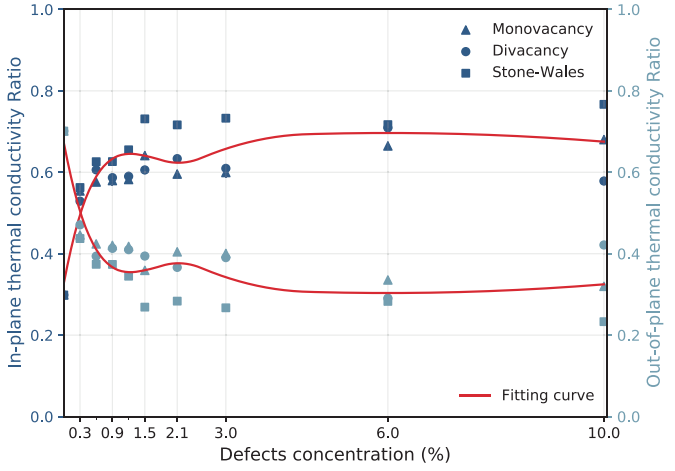

Fig. 8. Relationship between the percentage of in-plane and out-of-plane results for the thermal conductivity of defective 2D-PANI and the defects concentration. Each data point was obtained by averaging the results of the corresponding three independent simulations in Fig. 7. Specifically, the shape of the data points is used to differentiate between the three different types of defects - monovacancy, divacancy, and SW defects - and the color is used to differentiate between in-plane and out-of-plane percentage situations. The red curve is the result of a polynomial fitting of the in-plane and out-of-plane results respectively.

ous HNEMD, EMD and SHC methods. As the defects concentration gradually increased, the in-plane thermal conductivity component showed a general trend of first increasing rapidly and then gradually stabilizing. Specifically, from the fitting results, the in-plane component of the thermal conductivity stabilized to almost two-thirds when the defects concentration rose to 3% and beyond. This also means that the defects have a much weaker effect on the out-of-plane component of the thermal conductivity than the in-plane component.

In order to further understand the physical mechanisms underlying the weakening on the thermal conductivity of 2D-PANI by defects, the following analysis was carried out from the phonon perspective as an entry point. Phonon density of states (PDOS), a classical method for characterizing phonon activity in materials, will be used for a representative study of three defective 2D-PANIs at concentrations of 3% and 10%. For each defects concentration case, three independent simulations were carried out with different defect distributions and these results were averaged, as was done in the calculation of the thermal conductivity calculation. Since the energy of phonons is essentially the energy of atomic vibrations, the PDOS in the frequency domain can be obtained by performing the following Fourier integral transform on the atomic velocity auto-correlation function (VACF):

$$PDOS_{i\alpha}(\omega) = \int_{-\infty}^{+\infty} \langle v_{i\alpha}(t) v_{i\alpha}(0) \rangle e^{-2\pi i \omega t} dt \quad (\alpha = x, y, z) \tag{18}$$

Where ω is the phonon frequency and $\langle v_\alpha(t) v_\alpha(0) \rangle$ is the VACF in the α direction of the atom i at the relevant time t. For the polarized PDOS of the 2D material in this study, the average value of PDOS in the x and y directions was taken as the overall in-plane PDOS and only in-plane and out-of-plane phonons were distinguished.

As shown in Fig. 9, for the pristine 2D-PANI, the in-plane PDOS showed two distinct peaks in the high frequency band around $48THz$, while the PDOS contribution in the low-frequency band at frequencies less than $30THz$ is mainly from the out-of-plane part. With the introduction of structural defects, the PDOS peaks in its high frequency band were significantly damped, which was manifested by a sharp reduction in peak and a broadening of the bandwidth. The inhibition effect became more pronounced as the defects concentration increased. Without exception, the PDOS peak in the low-frequency bands also suffered from the weakening effect caused by the defects, but this effect was much less than that suffered by the high-frequency bands. These changes reflect the scattering effect of defects on phonons, which shortens the lifetime

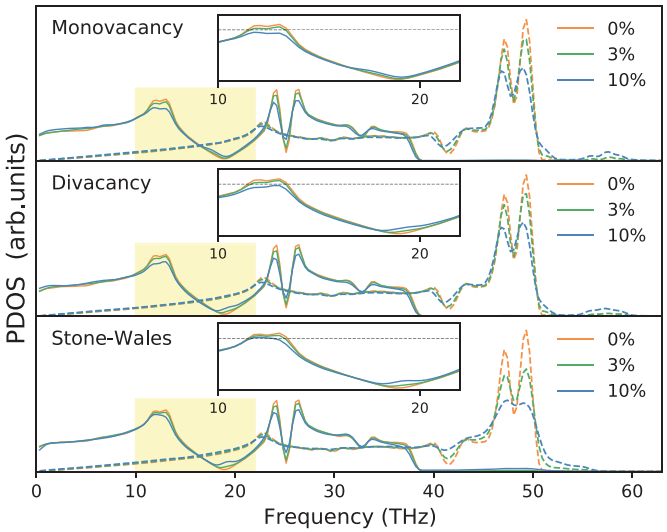

Fig. 9. Variation of phonon density of states (PDOS) with phonon frequency for the pristine and three defective 2D-PANIs at concentrations of 3% and 10%. The dashed line shows the in-plane part of the PDOS and the solid line shows the out-plane part. Further, a representative portion of the low-frequency band with a frequency of $10 \sim 22THz$ (shaded in yellow) is shown in detail in the inset, where the dotted line is a reference line corresponding to the same PDOS amplitude.

of phonons, and are reflected in the weakening effect on thermal conductivity. Combined with the HNEMD-based SHC thermal conductivity results in Fig. 5(a), it is known that the contribution to thermal transport comes mainly from the low-frequency acoustic modes less than 30 THz, and this part is dominated by out-of-plane PDOS. To this end, the insets in Fig. 9 showed representative enlargements of the out-of-plane PDOS results for the low-frequency bands in $10 \sim 22THz$, supplemented by reference lines for qualitative comparison. Overall, the difference between the calculated PDOS values for the same concentration of monovacancy and divacancy defects was very small, which provides strong support for the similar thermal conductivity results for both. However, the damping effect of the SW defect on the low-frequency out-of-plane PDOS of the 2D-PANI was significantly smaller than that of the vacancy defects at the same concentration. This also explains why the thermal conductivity of defective 2D-PANI with SW defects was obviously higher than that with vacancy defects at the same defects concentration in Fig. 7. From the above qualitative analysis, it can be concluded that the damping effect of defects on the low-frequency out-of-plane PDOS of 2D-PANI is the main cause of its reduced thermal conductivity, which makes a specific study for this particular part of the phonon imperative.

Next, the mechanism of the effect of the defect type and its concentration on the thermal conductivity of 2D-PANI will be explored in more depth by phonon localization effects. The phonon localization effect caused by structural defects, a common phenomenon in thermal transport processes, can be reflected by phonon participation rate (PPR) results. Without the lattice dynamics calculations, the PPR can be calculated directly by MD simulations at target temperatures, which can implicitly include anharmonic scattering of all-orders [49]:

$$PPR(\omega) = \frac{1}{N} \frac{\left(\sum_i PDOS_i^2(\omega)\right)^2}{\sum_i PDOS_i^4(\omega)} \tag{19}$$

where $PDOS_i(\omega)$ is the local PDOS of the atom i by Eq. (18) and N is the total number of atoms involved in the calculation. The PPR can be understood as the fraction of atoms participating in a certain mode ω, which provides a clearer and more intuitive picture of phonon participation at a given frequency. Since there is no clear correspondence in substance between the direction of vibration and the direction of energy propagation, that is, a vibration in a particular direction causes the propagation of two parts of energy along and perpendicular to that direction. Moreover, due to the higher group velocity of acoustic mode phonons (low-frequency band) than optical mode phonons (high-frequency band), their heat carrier efficiency is higher and they make the majority of the contribution to thermal transport. Therefore, in the quantitative calculation and analysis of the PPR, the low-frequency acoustic phonon modes from $0 \sim 30THz$ will be mainly considered, without further differentiation in direction.

Then, PPRs were calculated at 300 K for all 2D-PANI samples consistent with those calculated in Fig. 7, where each PPR result was obtained by statistical averaging of three independent simulations. Figs. 10(a-c) showed representative results of PPR calculations for three defective 2D-PANI with defects concentrations of 3% and 10%, compared to the pristine samples. Unsurprisingly, the weakening of the PPR by the defects covered the entire frequency domain without exception and had a more significant weakening effect at higher defects concentrations, which agrees perfectly with the PDOS results in Fig. 9. To further quantify the weakening effect of defects on PPR, the variation of average PPR with defects concentration in the low-frequency band for the three defective 2D-PANIs was statistically presented in Fig. 10(d), which covered acoustic mode phonons with frequencies from $0 \sim 30THz$. It is clear that the defects disturb the original atomic vibrational state of the whole system. It reduced the number of low-frequency phonons, which were responsible for the main thermal transport, and even caused phonon localization effects, which greatly reduced the thermal conductivity of the samples. In addition, the low-frequency average PPR decreased monotonically with increasing defects concentration, which explains the trend of gradually decreasing thermal conductivity with increasing defects concentration. It is noteworthy that monovacancy and divacancy defects showed an almost uniform effect on the respective low-frequency PPR. However, the SW defects exhibited significantly less weakening strength to the low-frequency PPR than the previous two, which reveals the underlying reason for the difference in thermal conductivity of the three defective 2D-PANIs at the same concentration.

3.2.2. Effect of temperature

In the study of the thermal transport properties of 2D materials, it is often essential to consider the effect of temperature, a physical quantity that is closely related to heat, on thermal conductivity. Three types of defective 2D-PANI with the size of $25nm \times 25nm$ and the defects concentrations of 0.3% and 3% respectively were used as basic samples and their respective thermal conductivities were calculated at five temperatures of 100K, 200K 300K, 400K, and 500K as shown in Fig.11. These temperature conditions range from low to high temperatures essentially covering all potential application scenarios for 2D-PANI.

In agreement with previous findings, the thermal conductivity results for defective 2D-PANI with two vacancy defects are almost indistinguishable under the same conditions, yet significantly different from that with topological defects. First, from an overall perspective, the thermal conductivity of each defective 2D-PANI showed a different downward trend as the temperature increased. This is due to the fact that high temperatures intensify lattice vibrations while enhancing anharmonic phonon-phonon scattering, that is Umklapp scattering, which is an important source of thermal resistance in micro-nano-scale materials. Next, the weakening effect of vacancy and topological defects on the thermal conductivity of 2D-PANI at different temperatures was compared. It is not difficult to find that at lower temperature conditions, the thermal conductivity of defective 2D-PANI with the same concen-

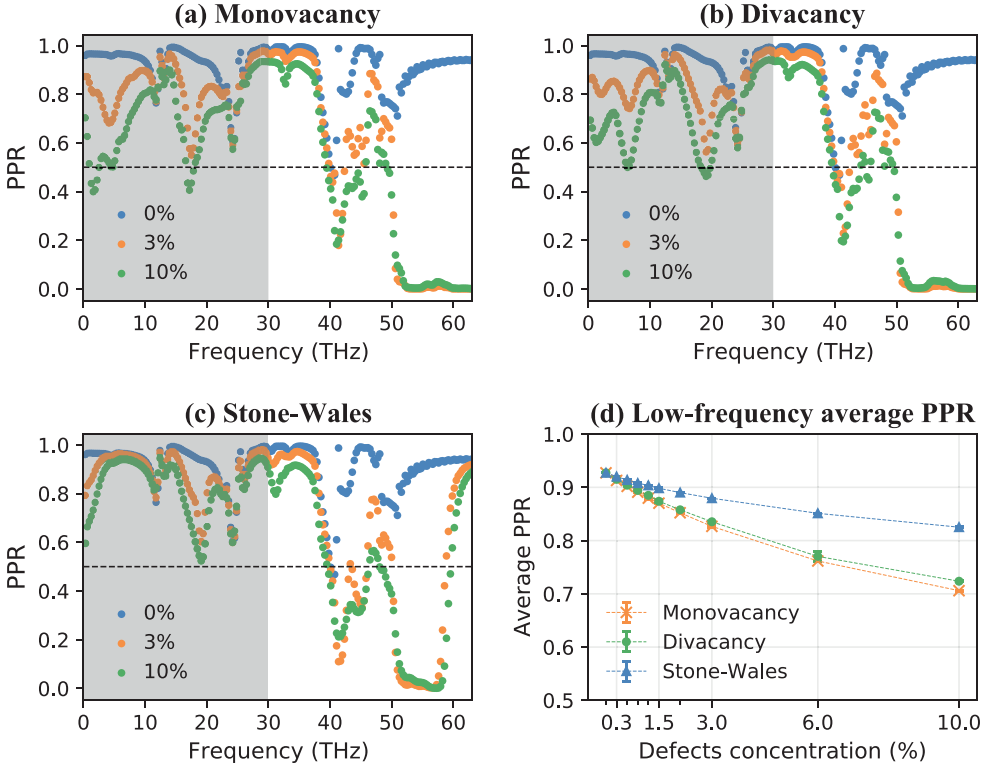

Fig. 10. Phonon participation rates (PPRs) versus phonon frequency for (a) monovacancy, (b) divacancy, and (c) SW three defective 2D-PANIs with defects concentrations of 3% and 10% at 300 K, respectively, which also include a comparison of each with the pristine case. The grey shaded area covers the low-frequency region from $0 \sim 30THz$ and the black horizontal dashed line is the reference line for the $PPR = 0.5$. (d) The relationship between the low-frequency average PPR of defective 2D-PANI and the defects concentration with the above three defects, where the error bars were calculated from the standard deviation of three independent simulations similar to the PDOS calculation.

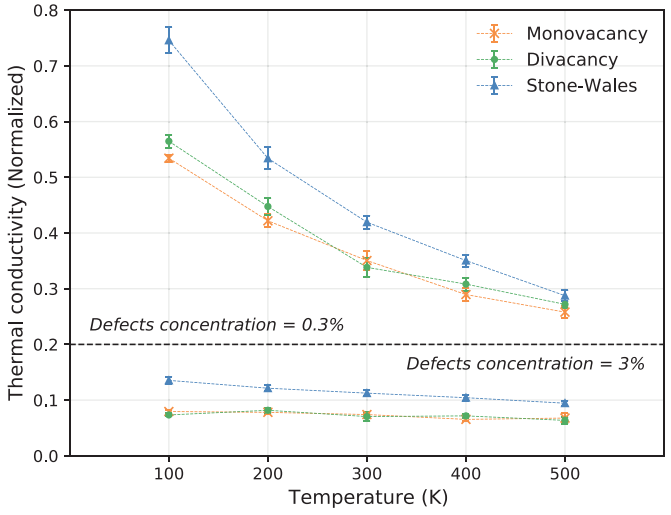

Fig. 11. Normalized thermal conductivity versus system temperature for three defective 2D-PANIs with defects concentrations of 0.3% and 3%, respectively. The normalized value of thermal conductivity is with respect to the value of pristine 2D-PANI at 300K. The dotted line is the dividing line between the two defects concentration cases, with the top and bottom of the dotted line corresponding to thermal conductivity results for defects concentrations of 0.3% and 3% respectively. The error bars were calculated by the standard deviation of the results of three thermal conductivity calculations for samples with different randomly distributed defects.

tration of topological defects was significantly higher than that of the case with vacancy defects. However, as the temperature increased, the difference between the thermal conductivity of the two types of defective 2D-PANI became smaller and smaller. This means that while the phonon-phonon scattering caused by high temperature dominates the weakening effect of thermal conductivity, it also weakens the difference in the effect of vacancy and topological defects on thermal conductivity. Then, the difference in the variation of defective 2D-PANI thermal conductivity with temperature at high and low defects concentrations was compared. The thermal conductivity of low-concentration defective 2D-PANI decreased significantly as the temperature increased, while this change was not obvious in high-concentration defective 2D-PANI. Although Umklapp scattering has a strong temperature dependence due to the increase in phonon population at high temperatures, phonon-defect scattering, which is largely dependent on defects concentration, is largely independent of temperature. We can conclude that as the defects concentration increases, phonon-defect scattering gradually dominates while weakening the temperature dependence of its thermal conductivity.

From the above analysis, it is easy to see that defect and temperature are two important factors affecting the thermal transport of 2D-PANI, mainly corresponding to phonon-defect scattering and phonon-phonon scattering respectively. The mutually restrictive nature of the two, such as the weak difference in the effect of defect types on thermal conductivity at high temperatures, and the insensitivity of high-concentration defective samples to temperature, may stimulate some novel applications of 2D-PANI in the field of thermal management.

4. Conclusion

To summarize, in this paper, we have performed large-scale MD simulations to calculate the thermal conductivity of infinitely large pristine 2D-PANI by three different versions of the method. The effect of three common structural defects, monovacancy, di-

vacancy, and SW defects, on the thermal transport properties of 2D-PANI has also been investigated by the HNEMD method. It has been found that the thermal conductivity of defective 2D-PANI has a low-power law dependence on the defects concentration and that vacancy defects have a stronger weakening effect on the thermal conductivity of the pristine material than topological defects at the same concentration. This is due to the fact that different types of defects bring about different phonon-defect scattering, which can be indirectly reflected by the low-frequency out-of-plane phonons which make the main contribution to thermal transport. For the anharmonic phonon-phonon scattering, which is strongly correlated with temperature, a potential constraint relationship with phonon-defect scattering has also been found. These above findings provide a new understanding of the behavior of thermal transport in 2D-PANI, which we hope will be useful for its future practical application.

Declaration of Competing Interest

The authors declared that they have no conflicts of interest to this work. We declare that we do not have any commercial or associative interest that represents a conflict of interest in connection with the work submitted.

CRediT authorship contribution statement

Xin Wu: Conceptualization, Methodology, Software, Validation, Formal analysis, Investigation, Writing - original draft, Writing - review & editing, Visualization. **Qiang Han:** Resources, Supervision, Project administration, Funding acquisition.

Acknowledgments

The authors are grateful for support from the National Natural Science Foundation of China (11972160, 11772130), Science and Technology Program of Guangzhou, China (202002030367).

References

[1] A.K. Geim, K.S. Novoselov, The rise of graphene, Nat. Mater. 6 (2007) 183–191, doi:10.1142/9789814287005_0002.
[2] T.-A. Chen, C.-P. Chuu, S. Pan, C.-C. Tseng, C.-K. Wen, H.-S.P. Wong, S. Pan, R. Li, T.-A. Chao, W.-C. Chueh, Y. Zhang, Q. Fu, B.I. Yakobson, W.-H. Chang, L.-J. Li, Wafer-scale single-crystal hexagonal boron nitride monolayers on Cu (111), Nature 579 (2020) 219–223, doi:10.1038/s41586-020-2009-2.
[3] A.J. Mannix, X.-F. Zhou, B. Kiraly, J.D. Wood, D. Alducin, B.D. Myers, X. Liu, B.L. Fisher, U. Santiago, J.R. Guest, M.J. Yacaman, A. Ponce, A.R. Oganov, M.C. Hersam, N.P. Guisinger, Synthesis of borophenes: Anisotropic, two-dimensional boron polymorphs, Science 350 (2015) 1513–1516, doi:10.1126/science.aad1080.
[4] B. Radisavljevic, A. Radenovic, J. Brivio, V. Giacometti, A. Kis, Single-layer MoS_2 transistors, Nat. Nanotechnol. 6 (2011) 147–150, doi:10.1038/nnano.2010.279.
[5] G. Algara-Siller, N. Severin, S.Y. Chong, T. Bjçrkman, R.G. Palgrave, A. Laybourn, M. Antonietti, Y.Z. Khimyak, A.V. Krasheninnikov, J.P. Rabe, U. Kaiser, A.I. Cooper, A. Thomas, M.J. Bojdys, Triazine-Based Graphitic Carbon Nitride: a Two Dimensional Semiconductor, Angew. Chem.-Int. Edit. 53 (2014) 7450–7455, doi:10.1002/anie.201402191.
[6] J. Mahmood, E.K. Lee, M. Jung, D. Shin, I.-Y. Jeon, S.-M. Jung, H.-J. Choi, J.-M. Seo, S.-Y. Bae, S.-D. Sohn, N. Park, J.H. Oh, H.-J. Shin, J.-B. Baek, Nitrogenated holey two-dimensional structures, Nat. Commun. 6 (2015) 6486, doi:10.1038/ncomms7486.
[7] J. Mahmood, E.K. Lee, M. Jung, D. Shin, H.-J. Choi, J.-M. Seo, S.-M. Jung, D. Kim, F. Li, M.S. Lah, N. Park, H.-J. Shin, J.H. Oh, J.-B. Baek, Two-dimensional polyaniline (C_3N) from carbonized organic single crystals in solid state, Proc. Natl. Acad. Sci. U. S. A. 113 (2016) 7414–7419, doi:10.1073/pnas.1605318113.
[8] B. Mortazavi, Ultra high stiffness and thermal conductivity of graphene like C_3N, Carbon 118 (2017) 25–34, doi:10.1016/j.carbon.2017.03.029.
[9] S.U. Lee, R.V. Belosludov, H. Mizuseki, Y. Kawazoe, Designing Nanogadgetry for Nanoelectronic Devices with Nitrogen-Doped Capped Carbon Nanotubes, Small 5 (2009) 1769–1775, doi:10.1002/smll.200801938.
[10] S. Yang, W. Li, C. Ye, G. Wang, H. Tian, C. Zhu, P. He, G. Ding, X. Xie, Y. Liu, Y. Lifshitz, S.-T. Lee, Z. Kang, M. Jiang, C_3N A 2D Crystalline, Hole-Free, Tunable-Narrow-Bandgap Semiconductor with Ferromagnetic Properties, Adv. Mater. 29 (2017) 1605625, doi:10.1002/adma.201605625.
[11] X. Zhou, W. Feng, S. Guan, B. Fu, W. Su, Y. Yao, Computational characterization of monolayer C_3N: A two-dimensional nitrogen-graphene crystal, J. Mater. Res. 32 (2017) 2993–3001, doi:10.1557/jmr.2017.228.
[12] L.-B. Shi, Y.-Y. Zhang, X.-M. Xiu, H.-K. Dong, Structural characteristics and strain behavior of two-dimensional C_3N : First principles calculations, Carbon 134 (2018) 103–111, doi:10.1016/j.carbon.2018.03.076.
[13] W. Li, X. Dai, J. Morrone, G. Zhang, R. Zhou, Thickness dependent semiconductor-to-metal transition of two-dimensional polyaniline with unique work functions, Nanoscale 9 (2017) 12025–12031, doi:10.1039/c7nr03281a.
[14] J. Miao, H. Li, H. Qiu, X. Wu, J. Yang, Graphene/PANI hybrid film with enhanced thermal conductivity by in situ polymerization, J. Mater. Sci. 53 (2018) 8855–8865, doi:10.1007/s10853-018-2112-z.
[15] H. Wang, H. Jiang, Y. Hu, N. Li, X. Zhao, C. Li, 2D MoS_2/polyaniline heterostructures with enlarged interlayer spacing for superior lithium and sodium storage, J. Mater. Chem. A 5 (2017) 5383–5389, doi:10.1039/c7ta00030h.
[16] S. Kumar, S. Sharma, V. Babar, U. Schwingenschlogl, Ultralow lattice thermal conductivity in monolayer C_3N as compared to graphene, J. Mater. Chem. A 5 (2017) 20407–20411, doi:10.1039/c7ta05872a.
[17] B. Peng, B. Mortazavi, H. Zhang, H. Shao, K. Xu, J. Li, G. Ni, T. Rabczuk, H. Zhu, Tuning Thermal Transport in C_3N Monolayers by Adding and Removing Carbon Atoms, Phys. Rev. Appl. 10 (2018) 034046, doi:10.1103/PhysRevApplied.10.034046.
[18] X. Wu, Q. Han, Thermal conductivity of monolayer hexagonal boron nitride: From defective to amorphous, Comput. Mater. Sci. 184 (2020) 109938, doi:10.1016/j.commatsci.2020.109938.
[19] X. Wu, Q. Han, Thermal conductivity of defective graphene: an efficient molecular dynamics study based on graphics processing units, Nanotechnology 31 (2020) 215708, doi:10.1088/1361-6528/ab73bc.
[20] Y. Dong, M. Meng, M.M. Groves, C. Zhang, J. Lin, Thermal conductivities of two-dimensional graphitic carbon nitrides by molecule dynamics simulation, Int. J. Heat Mass Transf. 123 (2018) 738–746, doi:10.1016/j.ijheatmasstransfer.2018.03.017.
[21] J. Song, Z. Xu, X. He, Y. Bai, L. Miao, C. Cai, R. Wang, Thermal conductivity of two-dimensional BC_3: a comparative study with two-dimensional C_3N, Phys. Chem. Chem. Phys. 21 (2019) 12977–12985, doi:10.1039/c9cp01943j.
[22] S.M. Hatam-Lee, A. Rajabpour, S. Volz, Thermal conductivity of graphene polymorphs and compounds: From C_3N to graphdiyne lattices, Carbon 161 (2020) 816–826, doi:10.1016/j.carbon.2020.02.007.
[23] S. Plimpton, Fast Parallel Algorithms for Short-Range Molecular Dynamics, J. Comput. Phys. 117 (1993) 1–19, doi:10.2172/10176421.
[24] Z. Fan, L.F.C. Pereira, H.-Q. Wang, J.-C. Zheng, D. Donadio, A. Harju, Force and heat current formulas for many-body potentials in molecular dynamics simulations with applications to thermal conductivity calculations, Phys. Rev. B 92 (2015) 094301, doi:10.1103/PhysRevB.92.094301.
[25] P. Boone, H. Babaei, C.E. Wilmer, Heat Flux for Many-Body Interactions: Corrections to LAMMPS, J. Chem. Theory. Comput. 15 (2019) 5579–5587, doi:10.1021/acs.jctc.9b00252.
[26] D. Surblys, H. Matsubara, G. Kikugawa, T. Ohara, Application of atomic stress to compute heat flux via molecular dynamics for systems with many-body interactions, Phys. Rev. E 99 (2019) 051301(R), doi:10.1103/PhysRevE.99.051301.
[27] A.W. Robertson, C. s. Allen, Y.A. Wu, K. He, J. olivier, J. neethling, A.I. Kirkland, J.H. Warner, Spatial control of defect creation in graphene at the nanoscale, Nat. Commun. 3 (2012) 1144, doi:10.1038/ncomms2141.
[28] A. Arora, T. Hori, T. Shiga, J. Shiomi, Thermal rectification in restructured graphene with locally modulated temperature dependence of thermal conductivity, Phys. Rev. B 96 (2017) 165419, doi:10.1103/PhysRevB.96.165419.
[29] D.J. EVANS, Homogeneous NEMD Algorithm for Thermal Conductivity Application of Non-canonical Linear Response Theory, Phys. lett. 91 (1982) 457–460, doi:10.1016/0375-9601(82)90748-4.
[30] M.S. Green, Markoff Random Processes and the Statistical Mechanics of Time-Dependent Phenomena. II. Irreversible Processes in Fluids, J. Chem. Phys. 22 (1954) 398, doi:10.1063/1.1740082.
[31] R. Kubo, Statistical-Mechanical Theory of Irreversible Processes. I. General Theory and Simple Applications to Magnetic and Conduction Problems, J. Phys. Soc. Jpn. 12 (1957) 570–586, doi:10.1143/JPSJ.12.570.
[32] K. Sääskilahti, J. Oksanen, J. Tulkki, S. Volz, Role of anharmonic phonon scattering in the spectrally decomposed thermal conductance at planar interfaces, Phys. Rev. B 90 (2014) 134312, doi:10.1103/PhysRevB.90.134312.
[33] Z. Fan, L.F.C. Pereira, P. Hirvonen, M.M. Ervasti, K.R. Elder, D. Donadio, T. Ala-Nissila, A. Harju, Thermal conductivity decomposition in two-dimensional materials: Application to graphene, Phys. Rev. B 95 (2017) 144309, doi:10.1103/PhysRevB.95.144309.
[34] Z. Fan, H. Dong, A. Harju, T. Ala-Nissila, Homogeneous nonequilibrium molecular dynamics method for heat transport and spectral decomposition with many-body potentials, Phys. Rev. B 99 (2019) 064308, doi:10.1103/PhysRevB.99.064308.
[35] A. Kınacı, J.B. Haskins, C. Sevik, T. Çağın, Thermal conductivity of bn-c nanostructures, Phys. Rev. B 86 (2012) 115410, doi:10.1103/PhysRevB.86.115410.
[36] K.K. Mandadapu, R.E. Jones, P. Papadopoulos, A homogeneous nonequilibrium molecular dynamics method for calculating thermal conductivity with a three-body potential, J. Chem. Phys. 130 (2009) 204106, doi:10.1063/1.3141982.

[37] K. Sääskilahti, J. Oksanen, S. Volz, J. Tulkki, Frequency-dependent phonon mean free path in carbon nanotubes from nonequilibrium molecular dynamics, Phys. Rev. B 91 (2015) 115426, doi:10.1103/PhysRevB.91.115426.
[38] P.K. Schelling, S.R. Phillpot, P. Keblinski, Comparison of atomic-level simulation methods for computing thermal conductivity, Phys. Rev. B 65 (2002) 144306, doi:10.1103/PhysRevB.65.1443062002.
[39] Z. Fan, T. Siro, A. Harju, Accelerated molecular dynamics force evaluation on graphics processing units for thermal conductivity calculations, Comput. Phys. Commun. 184 (2013) 1414–1425, doi:10.1016/j.cpc.2013.01.008.
[40] Z. Fan, W. Chen, V. Vierimaa, A. Harju, Efficient molecular dynamics simulations with many-body potentials on graphics processing units, Comput. Phys. Commun. 10–16 (2017) 218, doi:10.1016/j.cpc.2017.05.003.
[41] L. Lindsay, D.A. Broido, Optimized tersoff and brenner empirical potential parameters for lattice dynamics and phonon thermal transport in carbon nanotubes and graphene, Phys. Rev. B 81 (2010) 205441, doi:10.1103/PhysRevB.81.205441.
[42] S. Bazrafshan, A. Rajabpour, Engineering of thermal transport in graphene using grain size, strain, nitrogen and boron doping; a multiscale modeling, Int. J. Heat Mass Transf. 123 (2018) 534–543, doi:10.1016/j.ijheatmasstransfer.2018.02.107.
[43] A. Shirazi, R. Abadi, M. Izadifar, N. Alajlan, T. Rabczuk, Mechanical responses of pristine and defective C_3N nanosheets studied by molecular dynamics simulations, Comput. Mater. Sci. 147 (2018) 316–321, doi:10.1016/j.commatsci.2018.01.058.
[44] I.M. Felix, L.F.C. Pereira, Thermal conductivity of graphenehbn superlattice ribbons, Sci. Rep. 8 (2018) 2737, doi:10.1038/s41598-018-20997-8.
[45] A.J.C. Ladd, B. Moran, Lattice thermal conductivity: A comparison of molecular dynamics and anharmonic lattice dynamics, Phys. Rev. B 34 (1986) 5058–5064, doi:10.1103/PhysRevB.34.5058.
[46] A. FASOLINO, J.H. LOS, M.I. KATSNELSON, Intrinsic ripples in graphene, Nat. Mater. 6 (2007) 858–861, doi:10.1038/nmat2011.
[47] S. Sadeghzadeh, Effects of vacancies and divacancies on the failure of C_3N nanosheets, Diam. Relat. Mat. 89 (2018) 257–265, doi:10.1016/j.diamond.2018.09.018.
[48] S. Sadeghzadeha, M. Ghojavandb, J. Mahmoudi, Influence of stone-wales defects on the mechanical properties of graphenelike polyaniline (pani) C_3N nanosheets, Diam. Relat. Mat. 101 (2020) 107555, doi:10.1016/j.diamond.2019.107555.
[49] G. Loh, E. Teo, B. Tay, Phonon localization around vacancies in graphene nanoribbons, Diam. Relat. Mat. 23 (2012) 88–92, doi:10.1016/j.diamond.2012.01.006.